

# Thermo-optical dynamics in an optically pumped Photonic Crystal nano-cavity

M. Brunstein<sup>1</sup>, R. Braive<sup>1</sup>, R. Hosten<sup>1</sup>, A. Beveratos<sup>1</sup>, I. Robert-Philip<sup>1</sup>, I. Sagnes<sup>1</sup>,  
T. J. Karle<sup>1</sup>, A. M. Yacomotti<sup>1,\*</sup>, J. A. Levenson<sup>1</sup>, V. Moreau<sup>1,2</sup>, G. Tessier<sup>2</sup> and  
Y. De Wilde<sup>2</sup>

<sup>1</sup> Laboratoire de Photonique et de Nanostructures (CNRS UPR20), Route de Nozay, 91460 Marcoussis, France  
<sup>2</sup> Institut Langevin, ESPCI ParisTech, CNRS UMR 7587, Laboratoire d'Optique Physique, 10 rue Vauquelin, 75 231  
Paris Cedex 05, France

\* [Alejandro.Giacomotti@lpn.cnrs.fr](mailto:Alejandro.Giacomotti@lpn.cnrs.fr)

**Abstract:** Linear and non-linear thermo-optical dynamical regimes were investigated in a photonic crystal cavity. First, we have measured the thermal relaxation time in an InP-based nano-cavity with quantum dots in the presence of optical pumping. The experimental method presented here allows one to obtain the dynamics of temperature in a nanocavity. It is based on reflectivity measurements of a cw probe beam coupled through an adiabatically tapered fiber. Characteristic times of  $1.0 \pm 0.2 \mu\text{s}$  and  $0.9 \pm 0.2 \mu\text{s}$  for the heating and the cooling processes were obtained. Finally, thermal dynamics were also investigated in a thermo-optical bistable regime. Switch-on/off times of  $2 \mu\text{s}$  and  $4 \mu\text{s}$  respectively were measured, which could be explained in terms of a simple non-linear dynamical representation.

©2008 Optical Society of America

**OCIS codes:** (190.4390) Nonlinear optics, integrated optics; (190.1450) Bistability; (130.3120) Integrated optics devices; (060.1810) Couplers, switches, and multiplexers.

---

## References and links

1. K. Hennessy, A. Badolato, M. Winger, D. Gerace, M. Atatüre, S. Gulde, S. Fält, E. L. Hu and A. Imamoglu, "Quantum nature of a strongly coupled single quantum dot-cavity system," *Nature* **445**, 896 (2007); S. Laurent, S. Varoutsis, L. Le Gratiet, A. Lemaître, I. Sagnes, F. Raineri, A. Levenson, I. Robert-Philip and I. Abram, "Indistinguishable single photons from a single quantum dot in two-dimensional Photonic Crystal cavity," *Appl. Phys. Lett.* **87**, 163107 (2005).
2. M. Notomi, T. Tanabe, A. Shinya, E. Kuramochi, H. Taniyama, S. Mitsugi, M. Morita, "Nonlinear and adiabatic control of high-Q photonic crystal nanocavities," *Opt. Express* **15**, 17458 (2007).
3. A. M. Yacomotti, F. Raineri, G. Vecchi, P. Monnier, R. Raj, J. A. Levenson, B. Ben Bakir, C. Seassal, X. Letartre, P. Viktorovitch, L. Di Cioccio, J.-M. Fedeli, "All-optical bistable band-edge Bloch modes in a two-dimensional photonic crystal," *Appl. Phys. Lett.* **88**, 231107 (2006).
4. T. Tanabe, M. Notomi, S. Mitsugi, A. Shinya, and E. Kuramochi, "All-optical switches on a silicon chip realized using photonic crystal nanocavities," *Appl. Phys. Lett.* **87**, 151112 (2005).
5. R. Braive, S. Barbay, I. Sagnes, A. Miard, I. Robert-Philip, and A. Beveratos, "Transient chirp in high-speed photonic-crystal quantum-dot lasers with controlled spontaneous emission," *Opt. Lett.* **34**, 554 (2009).
6. H. Altug, D. Englund, and J. Vuckovic, "Ultrafast photonic crystal nanocavity laser," *Nat. Phys.* **2**, 484 (2006).
7. Y. A. Vlasov, M. O'Boyle, H. F. Hamann and S. J. McNab, "Active control of slow light on a chip with photonic crystal waveguides," *Nature* **438**, 65 (2005).
8. T. J. Johnson, M. Borselli, and O. Painter, "Self-induced optical modulation of the transmission through a high-Q silicon microdisk resonator," *Opt. Express* **14**, 817-831 (2006).
9. T. Carmon, L. Yang, and K. J. Vahala, "Dynamical thermal behavior and thermal self-stability of microcavities," *Opt. Express* **12**, 4742 (2004).
10. A. M. Yacomotti, P. Monnier, F. Raineri, B. Ben Bakir, C. Seassal, R. Raj, and J. A. Levenson, "Fast Thermo-Optical Excitability in a Two-Dimensional Photonic Crystal," *Phys. Rev. Lett.* **97**, 143904 (2006).
11. M. T. Tinker and J.-B. Lee, "Thermal and optical simulation of a photonic crystal light modulator based on the thermo-optic shift of the cut-off frequency," *Optics Express* **18**, 7174-7187 (2005).
12. G. Tessier, G. Jerosolimski, S. Hole, D. Fournier, and C. Filloy, "Measuring and predicting the thermoreflectance sensitivity as a function of wavelength on encapsulated materials," *Rev. Sci. Instrum.* **74** (1), 495 (2003).

13. L. Pottier, "Micrometer scale visualization of thermal waves by photoreflectance microscopy," *Appl. Phys. Lett.* **64**, 1618-1619 (1994).
14. Y. Akahane, T. Asano, B.-S. Song and S. Noda, "High- $Q$  photonic nanocavity in a two-dimensional photonic crystal," *Nature* **425**, 944 (2003).
15. A. Michon, R. Hosten, G. Patriarche, N. Gogneau, G. Beaudoin, A. Beveratos, I. Robert-Philip, S. Laurent, S. Sauvage, P. Boucaud, I. Sagnes, "Metal organic vapor phase epitaxy of InAsP/InP(001) quantum dots for 1.55  $\mu\text{m}$  applications: Growth, structural, and optical properties," *J. Appl. Phys.* **104**, 043504 (2008).
16. I. Hwang, S. Kim, J. Yang, S. Kim, S. Lee, and Y. Lee, "Curved-microfiber photon coupling for photonic crystal light emitter," *Appl. Phys. Lett.* **87**, 131107 (2005)
17. P. E. Barclay, K. Srinivasan, M. Borselli, and O. Painter, "Probing the dispersive and spatial properties of photonic crystal waveguides via highly efficient coupling from fiber tapers," *Appl. Phys. Lett.* **85**, (2004)
18. C. Grillet, C. Smith, D. Freeman, S. Madden, B. L-Davies, E. C. Magi, D. J. Moss and B. J. Eggleton, "Efficient coupling to chalcogenide glass photonic crystal waveguides via silica optical fiber nanowires," *Opt. Express* **14**, 1070 (2006).
19. See for example B. Maes, P. Bienstman, and R. Baets, "Switching in coupled nonlinear photonic-crystal resonators," *J. Opt. Soc. Am. B* **22**, 1778 (2005).
20. In Section 5 we study nonlinear thermo-optical effects which are shown to appear for a signal power greater than  $\sim 1$  mW (see transmission curves as a function of input power in Fig. 4c).
21. M. Notomi, A. Shinya, S. Mitsugi, G. Kira, E. Kuramochi, and T. Tanabe, "Optical bistable switching action of Si high- $Q$  photonic-crystal nanocavities," *Opt. Express* **13**, 2678-2687 (2005).
22. P. Barclay, K. Srinivasan, and O. Painter, "Nonlinear response of silicon photonic crystal microresonators excited via an integrated waveguide and fiber taper," *Opt. Express* **13**, 801-820 (2005).
23. Convection within the air gap can be neglected since the Rayleigh number for an air gap of thickness  $\delta$  between two rigid walls, for a few degrees of temperature increment, is  $Ra_\delta = g \Delta T \delta^3 / \nu \alpha T \sim 10^{10}$ , whereas the onset for convection is  $Ra_\delta \sim 2 \cdot 10^3$ . See for example J. Taine and J. P. Petit, *Heat transfert* (Prentice-Hall, 1993).
24. F. G. Della Corte, G. Cocorullo, M. Iodice, and I. Rendina, "Temperature dependence of the thermo-optic coefficient of InP, GaAs, and SiC from room temperature to 600 K at the wavelength of 1.5  $\mu\text{m}$ ," *Appl. Phys. Lett.* **77**, 1614 (2000).
25. F. Raineri, G. Vecchi, A. M. Yacomotti, C. Seassal, P. Viktorovitch, R. Raj and A. Levenson, "Doubly resonant photonic crystal for efficient laser operation: Pumping and lasing at low group velocity photonic modes," *Appl. Phys. Lett.* **86**, 011116 (2005).
26. The thermal relaxation time for a PhC membrane on oxide can be easily calculated under the hypothesis of 1D vertical heat flow through the oxide layer to the substrate. For instance, for a 250 nm-thick Si membrane ( $\kappa_{\text{Si}} = 1.5$  W/cm K,  $\alpha_{\text{Si}} = 0.9$  cm<sup>2</sup>/s) in contact with a 1  $\mu\text{m}$ -thick SiO<sub>2</sub> layer ( $\kappa_{\text{SiO}_2} = 0.013$  W/cm K,  $\alpha_{\text{SiO}_2} = 0.006$  cm<sup>2</sup>/s), a numerical simulation of the 1D heat equation gives  $\tau_{\text{th}} = 950$  ns.
27. A. R. A. Chalcraft, S. Lam, D. O'Brien, T. F. Krauss, M. Sahin, D. Szymanski, D. Sanvitto, R. Oulton, M. S. Skolnick, A. M. Fox, and D. M. Whittaker, "Mode structure of the L3 photonic crystal cavity," *Appl. Phys. Lett.* **90**, 241117 (2007).
28. We use the estimated  $\tau_{\text{th}}$  from the experimental results,  $\tau_{\text{th}} \sim 110$  ns (see Section 6.1). This is an approximation since  $\tau_{\text{th}}$  depends on the geometry of the hot spot which, in the resonant case, is given by the cavity volume, different from the pumped region given by the surface illumination.
29. C. Sauvan, P. Lalanne and J.P. Hugonin, "Slow-wave effect and mode-profile matching in Photonic Crystal microcavities," *Phys. Rev. B* **71**, 165118 (2005).

## 1. Introduction

Active Photonic Crystal nanocavities have recently received much attention due to their importance for quantum optics and quantum electrodynamics [1], as well as for dynamical and nonlinear control of light in photonic circuits [2]. In particular, in the context of active semiconductor devices, silicon and III-V-based nanocavities have been shown to exhibit interesting optically induced gain/absorption properties leading to ultrafast switching and bistability, among others [3-6].

Photon emission and/or carrier induced nonlinearities are obtained through the excitation of electrons in semiconductor conduction bands. Electron-hole nonradiative recombination processes play a fundamental role in the relaxation of excited electronic populations. These are mediated by phonons which become source of heat. While heating turns out to be an unwanted effect in most photonic devices because of detrimental thermal loading (specially in photonic crystal suspended membranes), it can also be used as a mechanism for fast switching (up to 10 MHz-bandwidth) as long as the dimensions of optical cavities are small enough [7-9]. Moreover, in the context of novel non-linear dynamical mechanisms relying on multiple time-scale processes, it has been demonstrated that the so-called thermo-optical excitable dynamics may lead to repetition rates as high as 1 GHz [10].

It is worth pointing out that, in all the above situations, an insight into dynamics of heat dissipation is of central importance since it provides information about the characteristic time scales to take into account when pumping the sample in order to avoid heating up the material, i.e. by modulating the optical pump faster than the thermal relaxation time. In particular, quasi cw light injection for nonlinear operation or laser emission requires the pump pulse to be longer than the carrier recombination lifetime, but shorter than the thermal time. For instance, we have recently demonstrated optical bistability in a 2D PhC following this approach [3].

In the case of self-induced heating phenomena in micro and nano optical cavities (i.e., when the heat is produced by optical excitation of the resonant mode in the cavity) the characteristic heat dissipation times strongly depend on the cavity size. As it has been pointed out in [9], these scale with the characteristic cavity length, i.e. small cavities dissipate heat faster. The equilibrium temperature, in turn, scales with the inverse cavity length, mainly due to the reduced heat capacity of small cavities. Fast thermal processes are thus compatible with high thermal loading, showing the importance of thermal measurements in small cavities, such as photonic crystal nanocavities.

Thermal relaxation often involves several time scales. This is especially the case for complex geometries such as a air-bridge photonic crystal slabs, where thermal dynamical measurements are particularly relevant since: i) the heat sink is a complex process given by the actual three-dimensional structure; ii) if air holes are present, full calculations –for instance by means of finite element methods– can be rather cumbersome. Recently, the thermal response in photonic crystal devices has been simulated using a finite-elements method [11]. In this study, the device concept was a thermo-optical switch based on a W1 photonic crystal waveguide on silicon. Heating was produced by a pair of electrodes close to the W1. Such a device reaches a stationary temperature of 420° C after 20  $\mu$ s. Heating and cooling times of 5.6  $\mu$ s and 3.5  $\mu$ s at 90% and 10% of the final temperature, respectively, were found.

From the experimental point of view, while thermal loading can be estimated through measurements of thermally induced refractive index change, the thermal relaxation times cannot be obtained straightforwardly; so far, this has been done through parameter fitting from non-linear dynamical models [8,10]. This requires a complex set of equations coupling several variables, therefore the fitted relaxation time becomes model-dependent. In this work we present a novel method to directly measure the thermal time out of a photonic crystal nanocavity, based on time-resolved reflectivity within a tapered fiber-assisted optical coupling scheme.

Available thermal characterization techniques in semiconductor microchips have mainly been developed for microelectronics and concern both stationary profiles and dynamics. Stationary temperature profile measurement is a standard technique using infrared CCD cameras that allows quantification of thermal loading averaged over time [12]. Dynamical measurements of thermal diffusion coefficients on the microscale is also an available technique based on visualization of thermal waves by photoreflectance microscopy [13]. The technique we propose here focuses on thermal dynamics averaged in the optical volume of a resonator; in the case of a photonic crystal nanocavity, the spatial resolution is given by the cavity dimensions, of the order of one micrometer. In Section 2 we describe the photonic crystal sample and we report on the main optical features through photoluminescence experiments. Section 3 is devoted to the description of the taper-assisted coupling method for probing the PhC nanocavity. In Section 4 the thermal dynamical measurements are shown. In Section 5 we illustrate the thermo-optical dynamical phenomena in the context of bistable switches. Section 6 gives a discussion of the results as well as a comparison with thermal properties of other nano and microphotonic systems reported in the literature. Finally, the conclusions are given in Section 7.

## 2. Sample description and characterization

The sample is a 10  $\mu$ m  $\times$  50  $\mu$ m photonic crystal of air holes (triangular lattice with period  $a=465$  nm, holes radius= $0.3a$ ) in an InP suspended membrane (air gap size= $1.16 \mu$ m, Figs. 1a

and 1b), with a nanocavity in the center. The cavity is a modified L3 [14], where the two holes closing the cavity are shifted away by  $0.15a$  (see. Fig. 1c). The 262 nm-thick ( $\lambda/2n$ ) InP membrane incorporates a central single layer of self-assembled InAsP/InP quantum dots (QDs), whose density is  $1.5 \times 10^{10} \text{ cm}^{-2}$  and whose luminescence at 300 K is centered around  $1.55 \mu\text{m}$  with a 145-nm inhomogeneous broadening [15]. The whole structure, incorporating a GaInAs sacrificial layer under the InP, is grown by metalorganic chemical vapor deposition (MOCVD).

The QD photoemission is used to identify the cavity mode under incoherent pump @ 800 nm using a 100 fs-pulses, 80 MHz-repetition rate Ti:Sa laser. The resonant mode filters the QD luminescence, giving a spectral peak at 1490 nm; no laser effect was observed for these cavities. Due to their relatively large emission spectrum, and almost flat emission over the cavity tuning range, QDs are well suited as an active material in the framework of our study since their absorption/gain curves are less sensitive to temperature induced spectral shifts with respect to quantum wells. As a result, it will be a good approximation to neglect the effects of thermally induced electronic band shifts on the cavity mode. Thus, only refractive index change with temperature will be taken into account.

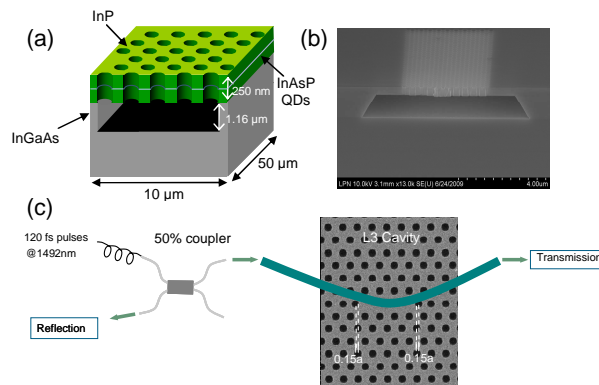


Fig. 1. (a). Sketch of the photonic crystal-membrane sample. (b). SEM cross-section image of a  $5 \mu\text{m}$ -width membrane showing the  $\sim 1 \mu\text{m}$ -thickness air gap. (c). Tapered fiber optical coupling scheme for transmission and reflectivity measurements. A SEM image of the L3 cavity is shown.

### 3. Taper-assisted coupling scheme

Once the optical mode is identified by looking at the photoluminescence, the cavity mode is probed resonantly through a curved tapered fiber (waist= $2 \mu\text{m}$  along  $500 \mu\text{m}$ , radius of curvature= $500 \mu\text{m}$ ), which can be approached to the cavity by means of a nanopositioning stage. The curvature of the taper reduces the optical coupling to the substrate outside the photonic crystal membrane, thus decreasing optical losses. The incident polarization angle with respect to the sample plane can be changed by means of a fiber polarization controller. Reflectivity measurements are well suited to probe the cavity resonance since they naturally avoid the uncoupled light background. In order to measure the reflection upon evanescent interaction between the taper and the cavity, a fibered 50% coupler is used. The coupling scheme, depicted in Fig. 1c, is similar to other approaches already reported for coupling light resonantly into W1 waveguides and cavities [16-18]. When the taper is positioned at the center of the defect in contact with the cavity, and broadband femtosecond pulses are injected into the fiber (120 fs pulses @ 1492 nm, linearly polarized), a reflected signal is detected showing a narrow peak (Fig. 2a, black line). This peak disappears when the taper is moved away from the cavity. The polarization angle is set to optimize the reflected signal.

In order to estimate the coupling efficiency, the transmission spectrum has been measured. This also shows a resonant feature at the same wavelength (Fig. 2b). We estimate the coupling efficiency using a simple model based on mode coupled theory [19]. Let  $\tau_c$  be the taper-cavity coupling time and  $\tau_0$  the cavity photon lifetime (defined for the field amplitude), the latter including the intrinsic cavity lifetime and other additional taper-induced cavity losses, such that  $\omega/2Q_{\text{loaded}}=1/\tau_0+1/\tau_c$ . The ratio of the –in resonance– transmitted power to the input power reads

$$\frac{|f_t|^2}{|f_i|^2} = \frac{1}{\left(1 + \frac{\tau_0}{\tau_c}\right)^2} \quad (1)$$

where  $|f_t|^2$  is the transmitted power in the vicinity of the cavity. The power measured at the fiber output is  $P_t=5.7$  nW. The transmitted power out of resonance is  $P_i\sim 11$  nW. Assuming  $|f_t|^2/|f_i|^2=P_t/P_i$  (frequency-independent intrinsic taper losses) we obtain  $|f_t|^2/|f_i|^2\approx 0.52$ , which gives  $\tau_0/\tau_c\approx 0.39$  using Eq. (1). We then define the coupling efficiency ( $\eta_c$ ) as the probability that a photon inside the cavity couples to the fiber (in either direction, hence  $P_c\propto 2/\tau_c$ ) with respect to the photon emission probability throughout all the coupling channels ( $P_{\text{tot}}\propto 2/\tau_c+1/\tau_0$ ), namely  $\eta_c\equiv P_c/P_{\text{tot}}=2/(2+\tau_c/\tau_0)$ . We point out that for an ideal coupling  $\tau_c\ll\tau_0$  which gives  $\eta_c\rightarrow 1$ . In our case we obtain a coupling efficiency of  $\eta_c=44\%$ . Let us stress that this high coupling efficiency is of great interest in many applications, like efficient single photon sources, or light extraction of cavity based nano-lasers.

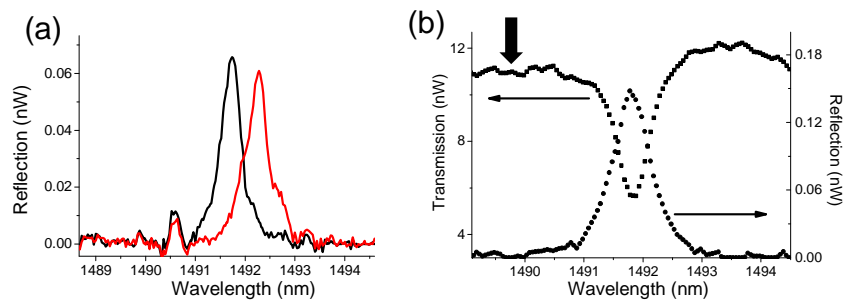


Fig. 2. (a). Reflectivity spectrum of the cavity resonance without pump (black line), and with  $165\mu\text{W}$  pump (red line). (b). Simultaneous transmission and reflection. The thick arrow indicates the out-of-resonance transmitted power used to estimate the coupling efficiency (see text).

#### 4. Thermal relaxation dynamics

First, the probe power injected into the taper was set to a low level ( $<1$  mW) in order to prevent any self-induced thermal or electronic effect [20]. In order to produce heat, the cavity is optically pumped by the surface using a modulated beam at  $800$  nm focused down to a  $3.2$   $\mu\text{m}$ -diameter spot ( $@1/e^2$  of the intensity). This wavelength is mainly absorbed in the InP (bandgap wavelength  $\sim 900\text{nm}$  @  $300$  K). Non-radiative carrier relaxation processes are the central mechanisms producing heat in the membrane. Thermal effects increase the refractive index, shifting the resonance to a longer wavelength. Figure 2a shows the resonance at  $165$   $\mu\text{W}$  pumping level on the sample.

Thermal dynamics is measured as follows. The wavelength of a tunable laser is set at a given detuning  $\Delta\lambda_0$  with respect to the resonance of the unpumped cavity ( $\Delta\lambda_0 \equiv \lambda_c - \lambda_p$ , where  $\lambda_c$  is the wavelength at the center of the resonance and  $\lambda_p$  the probe wavelength), probing the cavity-induced reflection. Heating up the cavity results in a thermally induced wavelength shift, producing a change in the reflected intensity of the probe light. A high sensitivity fiber-coupled avalanche photodiode (APD) with a 1.44 GHz-bandwidth is used to temporally resolve the change of the reflected signal. Traces are recorded on a 1 GHz -bandwidth oscilloscope. Upon 10  $\mu\text{s}$  width-50  $\mu\text{s}$  period square pump pulse excitation, the reflected signal exhibits either a drop-out followed by a recovery for  $\Delta\lambda_0 \geq 0$  (i.e. blue detuning), or intensity peaks for  $\Delta\lambda_0 < 0$  (red detuning). Both situations are directly related to the thermal dynamics of the resonance towards the equilibrium states. For a nearly resonant probe ( $\Delta\lambda_0 = 0$ , Fig. 3a), the signal decreases in the presence of the pump beam due to thermally-induced shift of the resonance. For red detuning, instead, the resonance “passes through” the injection wavelength leading to a maximum of intensity in the heating process, followed by a maximum in the cooling process (Figs. 3b-3d).

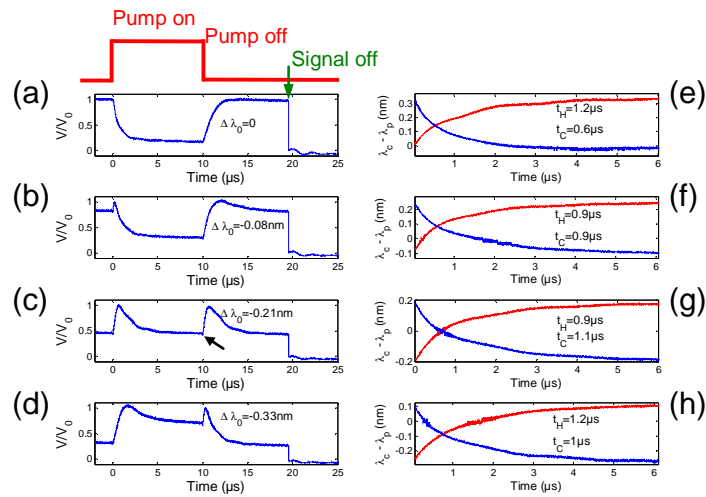


Fig. 3. Time dependence of the reflected cw probe upon squared pump modulation (red lines on top) for different detuning: a)  $\Delta\lambda_0=0$ ; b)  $\Delta\lambda_0=-0.08$  nm; c)  $\Delta\lambda_0=-0.21$  nm; d)  $\Delta\lambda_0=-0.33$  nm. (e)-(f) Thermal dynamics obtained from (a)-(d), taking into account the Lorentzian shape of the resonance. The arrow in (c) indicates a small amplitude short peak corresponding to electronic blue-shift dynamics before the slow thermal dynamics takes place.

In order to extract the characteristic thermal time from the time evolution of the reflected probe, the spectral shape of the resonance must be taken into account. The resonance can be fitted with a Lorentzian function. Considering the time dependence of the center of the resonance  $\lambda_c(t)$  –which contains the refractive index dependence with temperature–, the time-dependent reflectivity  $R(t)$  is thus modelled as  $R(t)=1/[1+(\lambda_c-\lambda_p)^2/(\gamma/2)^2]$ , where  $\gamma$  is the FWHM of the resonance. The resonance width  $\gamma$  has been measured from the reflectivity signals as a function of detuning, and gives  $\gamma=0.33$  nm, corresponding to a quality factor of  $Q_{\text{loaded}} \cong 4520$ . The time dependent wavelength shift becomes  $\Delta\lambda(t) \equiv \lambda_c(t) - \lambda_p = \pm [R(t)^{-1} - 1]^{1/2} \gamma/2$ , where the two roots indicate blue or red shift of the probe with respect to the cavity resonance. We point out that the kinetics of the center of the resonance also contains an ultrafast process related to carrier-induced index variation. By means of an ultrafast pump and probe technique we have verified that such processes decrease the refractive index blue-shifting the resonance in a time shorter than 1 ns, eventually being followed by a thermally driven red-shift. Therefore, they lead to short downward peaks, for red detuning, and short upward peaks for

blue detuning. We point out that such effects remain small in our measurements (see arrow in Fig. 3c).

Curves of  $\Delta\lambda(t)$  are plotted as a function of time in Figs. 3e-3h for the heating and cooling processes. Note the slight jumps in the signals at  $\Delta\lambda \sim 0$ , which are due to the discontinuity of the two roots in the inverse of the Lorentzian function. On the basis of such curves, the characteristic times have been calculated as the times at which the modulus of the total dynamical wavelength shift ( $|\lambda_c(t) - \lambda_c(t=0)| = |\Delta\lambda(t) - \Delta\lambda_0|$ ) becomes 1/e of its stationary value. As can be seen in Figs. 3e-3h, the heating and cooling times for the different detuning values are close to each other, as it is expected. Under the hypothesis that the characteristic times do not depend on the initial detuning, we average out the measured values for different detuning which yields  $t_c = 0.9 \pm 0.2 \mu\text{s}$  and  $t_H = 1.0 \pm 0.2 \mu\text{s}$  for the cooling and heating processes, respectively. We then conclude that there is no significant difference between cooling and heating times in the weak-probe regime. It is worth pointing out that for the zero-detuning case (Fig. 3e) the cooling time is about a factor 2 smaller compared to the other cases. For zero-detuning, indeed, the reflectivity time trace for the cooling process is mainly affected by the spectral tail at the blue side of the resonance, which is slightly different to the tail at the red side (see the slight asymmetry of the resonance in Fig. 2a), which may explain the substantial deviation for this situation. Therefore, our technique is more accurate for thermally-induced wavelength shifts within the FWHM of the resonance, i.e. far from the spectral tails ( $|\Delta\lambda(t)| < \gamma/2$ ).

## 5. Thermo-optical bistability

In this section we study the thermal dynamics in the context of bistable switches. Thermo-optical bistability [21-22] can be obtained through self-induced red shift of the resonance upon (large enough) cw injection from a single beam. Indeed, the thermally-induced refractive index increase also takes place for a nearly optically resonant cw injection, in absence of any incoherent pump. In such a case, bistable operation can be expected provided that: i) the injection wavelength is at the red side of the resonance; ii) the detuning between the injection beam and the cold resonance is larger (in modulus) than  $\sim \sqrt{3}\gamma/2$ ; iii) the injection power exceeds a given threshold. As long as the nonlinearity comes from a thermo-optical effect, the switching times should be related to the characteristic thermal relaxation time obtained before.

For injection powers greater than  $\sim 1$  mW, thermo-optical bistability was observed. Bistable behaviour can be shown by measurements of output power as a function of input power for different detuning, leading to hysteresis cycles. Figure 4a shows the spectral range of wavelength detuning used in this experiment. Importantly, the power sweep in such measurements must be quasi-stationary, i.e. the duration of the power ramp must be much longer than the thermal dissipation time. Injection modulation is thus introduced by a 10 kHz triangular amplitude modulation of the input beam. In such conditions, simultaneous input modulation and optical transmission through the taper were measured as a function of time, the latter using a DC-coupled 1 GHz photodiode (Fig. 4b). For  $|\Delta\lambda_0| > 0.35$  nm, hysteresis loops are observed (Fig. 4c). Their size increases for larger detuning-values, up to  $|\Delta\lambda_0| \sim 0.72$  nm where the maximum injection power remains below the bistability threshold. Switching times have been measured as the time widths between the minimum and the maximum of the switch processes. The switch on time is  $1.8 \mu\text{s}$ , whether the switch off time is  $4 \mu\text{s}$ . Both are of the order of the  $1 \mu\text{s}$  characteristic time obtained with the pump and probe technique.

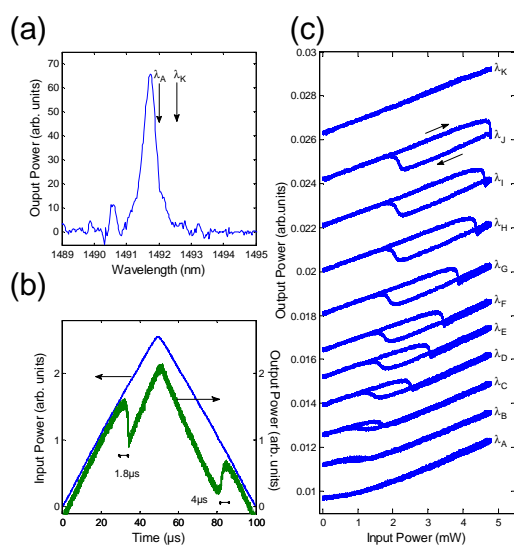


Fig. 4. Thermo-optical bistability. a) Reflectivity spectrum of the linear cavity resonance, and the wavelength range for the cw injection. b) Time traces of input (blue line) and transmitted output (green line) powers for a detuning of  $\Delta\lambda_0 = -0.56$ ; durations of the switch processes are  $1.8 \mu\text{s}$  and  $4 \mu\text{s}$  for the on/off switches respectively. c) Hysteresis cycles putting into evidence bistable behavior. Detuning-values with respect to the cavity resonance are, from  $\Delta\lambda_A$  to  $\Delta\lambda_K$ :  $-0.11, -0.27, -0.36, -0.46, -0.52, -0.56, -0.6, -0.64, -0.66, -0.68$  and  $-0.72$  nm. The input power is measured at the fiber taper input.

## 6. Discussion

### 6.1 Linear regime: thermal dynamics in a 2D PhC membrane

The energy absorbed in the pumped region can be essentially dissipated in two ways. The first mechanism of heat flow corresponds to heat conduction through the membrane (Fig. 5a). In order to obtain an analytical expression for the associated thermal resistance, let us consider a 2D cylindrical heat conductor of radius  $R$  with thermal conductivity  $\kappa$ , and a heat source of radius  $r$  (Fig. 5b). The thermal resistance for a length  $d$  (membrane thickness) between  $r$  and  $R$  is  $R_{\text{plane}} = \ln(R/r)/2\pi\kappa d \sim 1.7 \cdot 10^4$  K/W, where:  $R$  is half of the –smallest, i.e. closest to the heat sink– lateral size of the membrane ( $R = 5 \mu\text{m}$ ),  $r$  the pump radius ( $r = 1.6 \mu\text{m}$ ) and  $\kappa = \kappa_{\text{eff}} = 0.46$  W/cm K,  $\kappa_{\text{eff}}$  being an effective thermal conductivity calculated as a geometrical average of the material with holes. The second mechanism of heat flow corresponds to thermal conduction through the air gap [23]. This can be estimated as  $R_{\text{airgap}} = \delta/\kappa_{\text{air}} \pi r^2 \sim 6 \cdot 10^6$  K/W, where  $\delta$  is the air gap thickness ( $\delta = 1.16 \mu\text{m}$ ) and  $\kappa_{\text{air}} = 2.4 \cdot 10^{-4}$  W/cm K. Since  $R_{\text{airgap}} \gg R_{\text{plane}}$ , we can neglect heat transfer across the air gap and assume that the suspended membrane behaves as a quasi 2D system for heat diffusion and conduction. Eventually, heat is dissipated out of the membrane through the substrate. Now we derive the order of magnitude of the thermal time scale from a 2D heat equation. An analytical expression for the heat dissipation time in the quasi-stationary limit can be derived:  $\tau_{\text{th}} \approx \rho C_p r^2 \ln(R/r)/2\kappa$ , where  $\rho$  is the density and  $C_p$  the specific heat capacity in the pumped region. Using typical thermal constants for InP ( $\rho C_p = 1.5$  J/cm<sup>3</sup>K), we obtain  $\tau_{\text{th}} \sim 50$  ns. In order to compare the calculated  $\tau_{\text{th}}$  with the experimental results, we estimate  $\tau_{\text{th}}$  from the red shift of the resonance. We first calculate the temperature increase from tabulated values of refractive index change per unit temperature

( $n_T$ ,  $n_T/n \approx 0.63 \cdot 10^{-4} \text{ K}^{-1}$  @ 300 K for InP [24]) in the following way:  $\Delta T = (n/n_T) |\Delta \lambda_{\text{th}}/\lambda|$ . Using the measured red shift  $|\Delta \lambda_{\text{th}}| = 0.3 \text{ nm}$  with  $165 \mu\text{W}$  of incident power, we obtain  $\Delta T \approx 3.2 \text{ K}$ . Now, the temperature increase of the membrane under continuous pump can be related to  $\tau_{\text{th}}$  through  $\Delta T = \eta_{800} P_{\text{pump}} \tau_{\text{th}} / \rho C_p \text{Vol}$ , where  $\text{Vol} = \pi r^2 d$  ( $d$ =membrane thickness) is the volume of the pumped region and  $\eta_{800}$  is the fraction of the incident power absorbed at 800 nm ( $\eta_{800} \approx 33\%$  [25]). From the last expression we obtain  $\tau_{\text{th}} \approx 186 \text{ ns}$ .

Note that  $\tau_{\text{th}}$  is about one order of magnitude below the measured relaxation times. The difference between the thermal time scale for energy dissipation in the quasi-stationary limit and the relaxation time is related to a generic dynamical feature of heat diffusion in this kind of systems rather than just to the particularities of the photonic crystal. Indeed, such a difference has already been observed in other geometries without air holes such as microdisks [8]. In order to investigate the relaxation time  $t_{\text{th}}$ , let us look for the time dependent solutions of a 2D rectangular membrane of size  $2L_x \times 2L_y$  with thermal diffusivity  $\alpha$  and a heat source  $Q(\mathbf{r})$ , symmetric under reflections  $x \rightarrow -x$  and  $y \rightarrow -y$  (Fig. 5c). Boundary conditions are  $T(x=L_x) = T(y=L_y) = 0$  and  $\partial T/\partial x|_{x=0} = \partial T/\partial y|_{y=0} = 0$  for symmetrical solutions ( $T$  is temperature increase with respect to the substrate temperature). The general solution is a superposition of a particular (stationary) solution  $T_{\text{st}}(\mathbf{r})$  and the homogeneous solution,  $T(\mathbf{r}, t) = T_{\text{st}}(\mathbf{r}) + T_{\text{h}}(\mathbf{r}, t)$ . It can be easily showed that  $T_{\text{h}}$  can be expanded in Fourier series,

$$T_{\text{h}}(\mathbf{r}, t) = \sum_{n,m=0}^{\infty} A_{nm} e^{-\sigma_{nm} t} \cos(k_{xn} x) \cos(k_{ym} y) \quad (2)$$

with  $k_{xn} = (2n+1)\pi/2L_x$ ,  $k_{ym} = (2m+1)\pi/2L_y$  and  $\sigma_{nm}/\alpha = k_{xn}^2 + k_{ym}^2$ . The amplitudes  $A_{nm}$  can be obtained from the initial conditions. In the case of the heating process ( $Q(\mathbf{r}) \neq 0$ ) the initial condition is  $T^{(\text{H})}(\mathbf{r}, t=0) = 0$ , and the coefficients  $A^{(\text{H})}_{nm}$  are calculated as the Fourier transform of  $-T^{(\text{H})}_{\text{st}}(\mathbf{r})$ . Thus, the Fourier modes relax with characteristic times given by  $t_{\text{th},nm} = 4L_x^2 L_y^2 / \alpha \pi^2 [(2m+1)^2 L_x^2 + (2n+1)^2 L_y^2]$ . Note that higher order modes are dissipated faster. Therefore, we can expect the relaxation dynamics to be driven by the lowest order mode provided it is efficiently excited. In our case, since  $L_y \gg L_x$ ,  $t_{\text{th},00} \approx 4L_x^2 / \alpha \pi^2 \approx 300 \text{ ns}$ , meaning that the smallest length governs the relaxation process. This estimation is about a factor 3 below the measured relaxation time. In addition, Eq. 2 also accounts for cooling processes, whose dynamics is denoted by  $T^{(\text{C})}(\mathbf{r}, t)$ . In such a case the heat source is turned off ( $Q(\mathbf{r}) = 0$ ) hence  $T^{(\text{C})}_{\text{st}}(\mathbf{r}) = 0$  and the initial condition reads  $T^{(\text{C})}(\mathbf{r}, t=0) = T^{(\text{H})}_{\text{st}}(\mathbf{r})$ . Therefore  $A^{(\text{C})}_{nm} = -A^{(\text{H})}_{nm}$ , hence  $T^{(\text{C})}(\mathbf{r}, t) = -[T^{(\text{H})}(\mathbf{r}, t) - T^{(\text{H})}_{\text{st}}(\mathbf{r})]$ , which shows that the relaxation dynamics of the cooling process is the same as for the heating process.

The discrepancy between the experimentally obtained time constants  $\tau_{\text{th}}$  and  $t_{\text{th}}$  and their theoretical estimations may be due to the strong approximations used in our simple models, in particular the cylindrical symmetry to represent a 2D heat diffusion and conduction in the membrane, the effective conductivity of the photonic crystal as a simple spatial average of thermal conductivities, and the temperature being fixed to the ambient temperature at the end of the membrane (perfect heat sink at  $r=R$  in the cylindrical model, and at  $L_x$  and  $L_y$  in the rectangular model). Full 3D-finite element numerical simulations, as in Ref. [11], should be carried out in order to better account for thermal dynamics in this system.

The measured relaxation times are comparable to the numerical values obtained for a similar geometry in Ref. [11], where a slight asymmetry in turn-on/off processes has been observed. From the dynamical point of view, an asymmetry may arise if the system is heated during a time shorter compared to the characteristic heating time. In our case, since the pump-on and pump-off times  $\sim 10 \mu\text{s}$  and  $40 \mu\text{s}$  respectively are much longer compared to the relaxation time ( $\sim 1 \mu\text{s}$ ) we do not expect such an asymmetry. The difference in relaxation times with respect to Ref. [11] may be due to differences in size of the heated regions, membrane size, differences in thermal constants (the thermal conductivity of Si is about a factor 2 greater than the one of InP) and, most importantly, the presence of a  $1 \mu\text{m}$ -thick oxide layer underneath the PhC membrane. An oxide cladding is also present in Ref. [10], where the thermal relaxation time observed for a  $5 \mu\text{m}$ -size Bloch mode in a 2D InP PhC slab on  $\text{SiO}_2/\text{Si}$

was of the order of  $1 \mu\text{s}$  as well. In both cases, the lateral dimension of the heated region being quite large, the heat flow can be expected to be essentially driven by the  $\sim 1 \mu\text{m}$ -thickness  $\text{SiO}_2$  cladding directly to the substrate [26].

The Si-based PhC air-bridge membrane reported in [7] also exhibits characteristic times close  $1 \mu\text{s}$  for thermal effects, similar to our InP membrane in terms of lateral size. Finally, with respect to other geometries, we find our results comparable to the times found in silicon microdisks [8]. In the case of silica microdisks, in contrast, thermal dynamics lies on the millisecond timescale [9], mainly due to the low thermal diffusivity of silica; indeed, the thermal diffusivity ( $\kappa/\rho C_p$ ) is about two orders of magnitude smaller compared to silicon.

### 6.2 Nonlinear regime: thermo-optical bistability

In the nonlinear regime, the switching times were measured as the time interval between minimum and maximum of time traces. The obtained switching times are  $\sim 2 \mu\text{s}$  for the switch-on process (from the cold to the hot states), and  $\sim 4 \mu\text{s}$  from the switch-off process (from the hot to the cold states). As expected, both are related to the  $1 \mu\text{s}$  characteristic time measured in the linear regime.

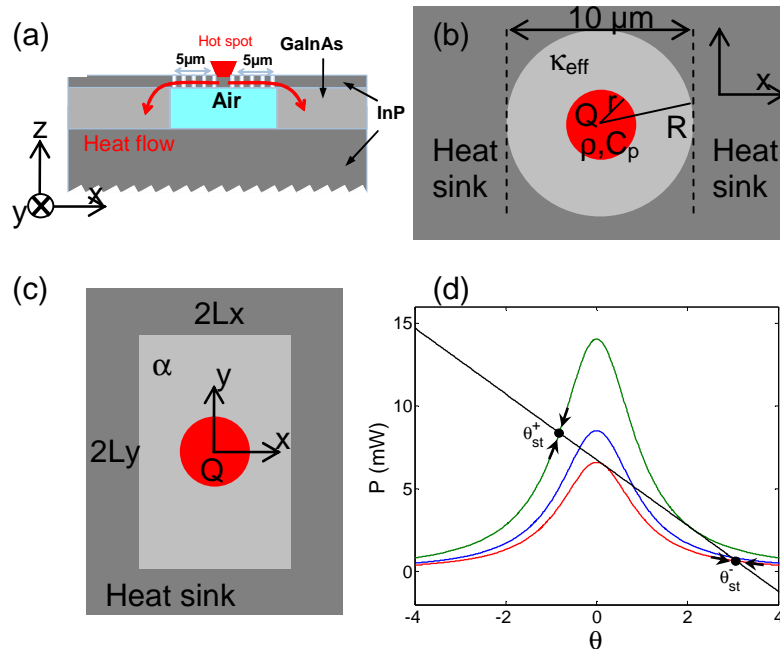


Fig. 5. (a). Sketch of the sample cross section, showing the direction of the heat flow. (b). Simplified model for cylindrical 2D heat conduction in a membrane;  $\kappa_{\text{eff}}$  represents the effective thermal conductivity of the photonic crystal membrane (see the definition of the other parameters in the text). (c). Rectangular geometry for the calculation of transient dynamics in a 2D membrane. (d). Phase space for bistability conditions. Blue, green and red lines: stationary solutions of the intracavity power ( $P$ ) as a function of the normalized wavelength shift ( $\theta$ ) for: bistable conditions ( $P_{\text{in,input}}=2 \text{ mW}$ , blue), switch on conditions ( $P_{\text{in,input}}=3.3 \text{ mW}$ , green) and switch off conditions ( $P_{\text{in,input}}=1.55 \text{ mW}$ , red). Black line: stationary solutions of  $\theta$ . The intersections of the black line with the curves give the steady states:  $\theta_{\text{st}}^{+(-)}$  is the stable state for the switch on (off) process. The direction of the dynamical flow is indicated by the arrows. The opposite slopes of  $dP/d\theta$  at the fixed points mathematically explain the difference in relaxation times (see text). Parameters are:  $P_0=2 \text{ mW}$  (calculated with  $V_c=0.08 \mu\text{m}^3$ ,  $\tau_{\text{th}}=186 \text{ ns}$ ,  $\Gamma=0.015$ ,  $Q_{\text{loaded}}=4520$ ,  $\eta_{1500}=0.00057$  and  $a=100 \text{ cm}^{-1}$ ),  $P_{\text{in}}=0.263 P_{\text{in,input}}$  ( $P_{\text{in,input}}$  is injected power into the fiber),  $\xi=16.2$  (using  $v_g=c/10$ , taken from Ref. [29]) and  $\theta_0=3.4$ .

The difference between switch-on and switch-off times can be explained from simple considerations of dynamical thermo-optical nonlinearities in the following way. The temperature variation  $\Delta T(t)$  imposes a dynamical thermal red shift  $|\Delta\lambda_{th}(t)/\lambda|=(n_T/n)\Delta T(t)$ , with  $\Delta T(t)=\eta_{1500}P(t)\tau_{th}/\rho C_p V_c$ , where:  $P(t)$  is the intracavity power;  $\eta_{1500}$  is the fraction of intracavity power absorbed at 1500 nm,  $\eta_{1500}\sim 2\Gamma aL$ , with  $\Gamma$  the optical confinement factor in the QDs layer,  $a$  the absorption coefficient and  $L$  is the cavity length;  $V_c$  is the cavity volume ( $V_c\sim 0.76(\lambda/n)^3$  [27]). Defining the normalized wavelength shift as  $\theta(t)=(\lambda_{in}-\lambda_c(t))/(\gamma/2)$ , where  $\lambda_{in}$  is the injection (rather than “probe” as in the linear case) wavelength, the dynamical equation becomes

$$\frac{d\theta(t)}{dt} = -\frac{1}{t_m} \left[ \theta(t) - \theta_0 + \frac{P(t)}{P_0} \right] \quad (3)$$

where  $P_0$  is a characteristic power inside the cavity,  $P_0=\rho C_p V_c/[2(n_T/n)Q_{loaded}\eta_{1500}\tau_{th}]$ ,  $t_m$  the characteristic relaxation time obtained in Section 4, and  $\tau_{th}$  the time scale for heat dissipation [28].

Since the dynamics of  $P(t)$  is much faster than the thermal processes, its dynamical equation can be adiabatically eliminated. Therefore  $P(t)$  becomes

$$P(t) = \frac{\xi P_{in}}{1 + \theta(t)^2}, \quad (4)$$

which simply describes the Lorentzian shape of the resonance ( $\xi$  is the intensification factor inside the cavity; this can be estimated from mode coupled theory to be  $\xi\sim v_g\tau_c/2L(1+\tau_c/\tau_0)^2$ , where  $v_g$  is the group velocity, and  $P_{in}$  is the input power in the vicinity of the cavity). The steady-state solutions can be graphically found by intersecting solutions of  $d\theta/dt=0$  from Eq. (3), and Eq. (4). Two stable states  $\theta_{st}^+$  and  $\theta_{st}^-$  coexist provided that  $\theta_0 > \sqrt{3}$ , and  $P_{in}>P_{th}$ , where  $P_{th}$  is the bistability threshold ( $P_{th}\sim P_0\theta_0/\xi$ , Fig. 5d). Steady state relaxation dynamics can be obtained through the linearization of Eq. 3 in the vicinity of the fixed points, i.e. by setting  $\theta\equiv\theta_{st}+A \exp(-t/\tau_{\pm})$  in Eq. (3). The eigenvalues  $\tau_{\pm}$  can be readily obtained:

$$\tau_{\pm}^{-1} = t_m^{-1} \left[ 1 + \frac{1}{P_0} \frac{dP}{d\theta} \Big|_{\theta_{st}^{\pm}} \right]. \quad (5)$$

Since  $P(t)$  has slopes with opposite signs at the two stable steady states (see Fig. 5d) corresponding to the switch on/off processes, namely positive (negative) slope for  $\theta_{st}^+$  ( $\theta_{st}^-$ ), therefore  $\tau_+<\tau_-$ , consistent with the experimental observation of switch-on times shorter than switch-off times. With the parameters of Fig. 5d we obtain  $\tau_+/\tau_-\approx 6.3$ . Experimentally, the ratio of switch-on to switch-off times was  $\sim 2.2$ , which contains the information of the full –i.e. nonlinear– relaxation dynamics, whereas the calculated  $\tau_+/\tau_-$  only accounts for the linear relaxation close to the steady states. We point out that the predicted difference in switching times given by Eq. (5) is generic in bistable systems and can be expected to hold even for fast nonlinearities. Moreover, even in absence of bistability, a high power input may affect the thermal dynamics in the way described by Eq. (5) leading to a dependence of the thermal relaxation times to the equilibrium state  $\theta_{st}$ . Unlike linear thermal dissipation regimes, in the nonlinear regime heating and cooling processes may have different relaxation times provided the intracavity power is close to the characteristic power  $P_0$ .

## 7. Conclusions

In conclusion, we have developed a method to directly measure the thermal relaxation time out of a photonic nanocavity. This technique relies on reflectivity measurements of a cw probe beam coupled to the cavity through a tapered fiber, becoming sensitive to the thermally induced increase of the refractive index within the cavity. We applied this method to an InP-based nanocavity on a suspended membrane. Wavelength shifts up to 0.3 nm for 165  $\mu$ W pumping power @ 800 nm were observed. The obtained values for the characteristic thermal times are close to 1  $\mu$ s, more than a factor 3 compared to a rough estimation of the relaxation time of the fundamental mode in a rectangular 2D membrane, showing the relevance of the experimental measurements. In addition, the thermal relaxation time has been shown to be closely related to switch on/off times within an opto-thermal bistable regime. In a general sense, additional engineering of photonic crystal geometries together with the inclusion of new materials should improve heat sink properties, which can be experimentally tested with the method proposed here. This would allow both increasing the repetition rate of thermal switches and reducing thermal loading for cw device operation. The latter is of central importance for obtaining fully stationary active and nonlinear functionalities such as efficient cw lasers and amplifiers, as well as long memories and logic gates based on cw bistable operation in photonic crystal circuits.

## Acknowledgments

These results are within the scope of C'Nano IdF and were supported by the Région Ile-de-France. C'Nano IdF is a CNRS, CEA, MESR and Région Ile-de-France Nanosciences Competence Center. We also thank R. Kuszelewicz, R. Raj and J.-J. Greffet for helpful discussions.